Are CMEs capable of producing Moreton waves? A case study: the 2006 December 6 event

G. Krause,[1,2,3]★ M. Cécere,[2,4,5]★ E. Zurbriggen,[2,4,5] A. Costa,[1,2,4]★ C. Francile[6] and S. Elaskar[1,2,3]

[1]*Facultad de Ciencias Exactas, Físicas y Naturales, Universidad Nacional de Córdoba (UNC), Córdoba X5016GCA, Argentina*
[2]*Consejo Nacional de Investigaciones Científicas y Técnicas (CONICET), C1033AAJ, Argentina*
[3]*Instituto de Estudios Avanzados en Ingeniería y Tecnología (IDIT), CONICET, Córdoba X5016GCA, Argentina*
[4]*Instituto de Astronomía Teórica y Experimental (IATE), CONICET-UNC, Córdoba X5000BGT, Argentina*
[5]*Observatorio Astronómico de Córdoba (OAC), UNC, X5000BGR, Argentina*
[6]*Observatorio Astronómico Félix Aguilar, Universidad Nacional de San Juan (UNSJ), San Juan, J5413FHL, Argentina*

ABSTRACT

Considering the chromosphere and a stratified corona, we examine, by performing 2D compressible magnetohydrodynamics simulations, the capability of a coronal mass ejection (CME) scenario to drive a Moreton wave. We find that given a typical flux rope (FR) magnetic configuration, in initial pseudo-equilibrium, the larger the magnetic field and the lighter (and hotter) the FR, the larger the amplitude and the speed of the chromospheric disturbance, which eventually becomes a Moreton wave. We present arguments to explain why Moreton waves are much rarer than CME occurrences. In the frame of the present model, we explicitly exclude the action of flares that could be associated with the CME. Analysing the Mach number, we find that only fast magnetosonic shock waves will be able to produce Moreton events. In these cases an overexpansion of the FR is always present and it is the main factor responsible for the Moreton generation. Finally, we show that this scenario can account for the Moreton wave of the 2006 December 6 event (Francile et al. 2013).

Key words: Sun: chromosphere – Sun: corona – Sun: coronal mass ejections (CMEs).

1 INTRODUCTION

Moreton waves are large-scale perturbations propagating at a chromospheric level. They were first detected by Moreton (1960) using H α observations. These waves propagate distances of the order of ∼500 Mm with linear velocities ranging from 500–2000 km s^{-1}. Due to the slow characteristic speeds of the chromosphere (of tens of km s^{-1}) in comparison with the larger typical Moreton speeds, it is now well established (Uchida 1968) that Moreton waves originate at a coronal level and not at the chromospheric one. Both flares and coronal mass ejections (CMEs) are impulsive coronal events capable of producing large-scale coronal shocks and therefore they are potential triggers of Moreton waves. Uchida (1968) and Uchida, Altschuler & Newkirk (1973) showed that a coronal shock produced by a flare can 'sweep' the chromospheric surface leading to a compression that could be associated with a Moreton phenomenon. Analysing flare events, Warmuth et al. (2001, 2004a,b), suggested that EUV Imaging Telescope (EIT) coronal waves are the counterpart of these chromospheric disturbances. Although there were discrepancies about the apparent velocity differences between the EIT and Moreton waves (Klassen et al. 2000; Asai et al. 2012) – which can be attributed to the poor temporal resolution of the observations and to the presence of multiple EUV wavefronts (e.g. Liu et al. 2010, Chen & Wu 2011) – numerous studies, including multiwavelength analysis, that cover a larger range of wave kinematics had led to the conclusion that EIT waves are the counterpart of Moreton events (e.g. Vršnak et al. 2002; Warmuth, Mann & Aurass 2005; Warmuth 2010). Moreover Shen & Liu (2012), found that high-cadence EUV observations have confirmed that both EUV and Moreton waves are triggered by the same disturbance.

Since CMEs and flares can be jointly observed, it is difficult to identify which phenomenon produces the Moreton wave. In order to distinguish the mechanisms that produce both phenomena, Vršnak & Cliver (2008) suggested that the propagation of a flare shock wave resembles the action of a piston (in which the ambient medium cannot move behind the piston and the shock wave can be faster than the piston speed). Meanwhile the evolution of a CME lift-off can be emulated by the combination of a piston (in its expansion) and a projectile (in its rising). A projectile generates a bow-shock with the same speed and the medium can flow behind it. With these considerations, Temmer et al. (2009) analytically interpreted that Moreton waves are generated either by the volume expansion of a flare or by the lateral motion of the CME flanks (given by its expansion) rather than by the upward motion of the CME front

★ E-mail: gustavo.krause@unc.edu.ar (GK); cecere@oac.unc.edu.ar (MC); acosta@oac.unc.edu.ar (AC)

(bow-shock). However, Francile et al. (2016), through an analysis of the observations of the 2014 March 29 event, found a large co-incidence between the initial ejection velocity of a filament (Kleint et al. 2015; Liu et al. 2015) and the expansion velocity of a quasi-spherical shock wave responsible for the Moreton wave, which suggests that a bow-shock mechanism could generate the disturbance in its initial stages.

Type II radio bursts (T2RBs) – generally coincident with Moreton waves – can help to understand the origin of the coronal event responsible for the chromospheric wave. However, while Vršnak et al. (2006), Narukage et al. (2008), Magdalenić et al. (2012) and Su et al. (2015) provided evidence that T2RBs related to Moreton waves are only produced by flares, due to the high energy that this phenomenon releases, Zucca et al. (2014) associated the detection of two T2RBs with a CME.

On the other hand, several numerical simulations have been carried out to explain the generation and evolution of Moreton waves in the frame of the flare and CME scenarios (Chen, Ding & Fang 2005; Wu, Wu & Liou 2013; Krause et al. 2015; Wang et al. 2015). In particular, Wang, Shen & Lin (2009) studied the capability of a CME to produce a chromospheric wave. They concluded that a CME can produce a Moreton wave, analysing the interaction between a fast coronal shock with a fixed boundary emulating the chromosphere. Recent numerical simulations of Vršnak et al. (2016) showed that an overexpanding flux rope (FR) can trigger a coronal large-amplitude fast magnetohydrodynamics (MHD) mode that is able to produce chromospheric perturbations like Moreton waves and other secondary effects.

The 2006 December 6 Moreton event, associated with both a CME and a flare, has been extensively studied. Balasubramaniam et al. (2010) proposed, through a kinematic study, that the CME flanks caused this Moreton wave. Studying the same event, Francile et al. (2013) proposed that the Moreton wave is produced by a coronal fast shock wave of a 'blast' type originating in a single source during a CME. They found that the event showed an overlap with the flare explosive phase and a small-scale ejecta ignition. In Krause et al. (2015) (hereafter Paper I) we simulated this particular Moreton wave and found that a piston mechanism could be at the base of the explanation of the phenomenon. We concluded that either a flare (simulated as an instantaneous piston) or the expansion of CME flanks (simulated through a temporary piston) can cause a Moreton wave. However, our scenario would not account for Moreton waves of higher speeds as in the 2014 March 29 event ($\sim$1200 km s^{-1}) described by Francile et al. (2016), i.e. for a faster wave a higher field strength would be required, which would then result in an amplitude that is too low to be compatible with observations (see Paper I).

In this work, as a continuation of the analysis in Paper I we now explore the CME scenario with an FR-type magnetic configuration (whose evolution could emulate the flank expansion – piston mechanism – and/or the bow-shock – projectile mechanism). We analyse as a particular case the event of 2006 December 6. Unlike Paper I, we here explicitly consider that any reconnection process (or flare associated with the CME) will allow the magnetic reconfiguration but will not determine the FR dynamics, i.e. only the CME lift-off is considered to be the driver of the Moreton wave.

2 THE MODEL

We implemented the 2D compressible resistive MHD equations considering gravity for a completely ionized hydrogen plasma, with $\gamma = 5/3$ (γ the ratio of specific heats) to study Moreton waves in the frame of a CME scenario:

$$\frac{\partial \rho}{\partial t} + \nabla \cdot (\rho \boldsymbol{u}) = 0, \tag{1}$$

$$\frac{\partial \rho \boldsymbol{u}}{\partial t} + \nabla \cdot (\rho \boldsymbol{u}\boldsymbol{u}) = -\nabla p + \frac{1}{c}\boldsymbol{j} \times \boldsymbol{B} + \rho \boldsymbol{g}, \tag{2}$$

$$\frac{\partial E}{\partial t} + \nabla \cdot [(E + p)\boldsymbol{u}] = \rho \boldsymbol{g} \cdot \boldsymbol{u} + \nabla \cdot (\boldsymbol{B} \times \eta c \boldsymbol{j}) - \nabla \cdot \boldsymbol{Q}, \tag{3}$$

$$\frac{\partial \boldsymbol{B}}{\partial t} = \nabla \times (\boldsymbol{u} \times \boldsymbol{B}) - \nabla \times \eta c \boldsymbol{j}, \tag{4}$$

where ρ indicates the plasma density, $\boldsymbol{u}$ the velocity, $\boldsymbol{B}$ the magnetic field, p is the pressure, $\boldsymbol{g}$ is the gravity acceleration, E is the total energy density given by

$$E = \frac{p}{(\gamma - 1)} + \frac{1}{2}\rho u^2 + \frac{B^2}{8\pi}, \tag{5}$$

and

$$\boldsymbol{j} = \frac{c}{4\pi}\nabla \times \boldsymbol{B} \tag{6}$$

is the current density, where c is the speed of light. The parameter η is the magnetic resistivity and $\boldsymbol{Q}$ is the conductive thermal flux. These equations are completed with the assumption of a perfect-gas law $p = 2\rho k_B T/m_i$, k_B being the Boltzmann constant, T the plasma temperature and m_i the proton mass. In addition, the divergence-free condition $\nabla \cdot \boldsymbol{B} = 0$ must be satisfied.

For the simulation of a CME we use a model that treats the current-carrying filament floating in the corona as an FR located at a height h_0 from the solar surface. The magnetic configuration consists of three components: the current-carrying FR, the mirror of the FR, and the background magnetic field produced by a dipole of relative intensity M. The initial magnetic field is given by (Forbes 1990):

$$B_x = B_\phi(R_-)(y - h_0)/R_- - B_\phi(R_+)(y + h_0)/R_+$$
$$- MdB_\phi(r + \frac{\Delta}{2})(r + \frac{\Delta}{2})[x^2 - (y + d)^2]/R_d^4,$$
$$B_y = -B_\phi(R_-)x/R_- + B_\phi(R_+)x/R_+$$
$$- MdB_\phi(r + \frac{\Delta}{2})(r + \frac{\Delta}{2})2x(y + d)/R_d^4, \tag{7}$$

with d the depth of the line dipole below the boundary surface and

$$R_\pm = \sqrt{x^2 + (y \pm h_0)^2},$$
$$R_d = \sqrt{x^2 + (y + d)^2}. \tag{8}$$

$B_\phi(R)$, the field oblique to the FR axis, is determined by the electric current density distribution $j(R)$ inside the FR in the z-direction:

$$B_\phi(R) = -\frac{2\pi}{c}j_0 R, 0 \leq R \leq r - \frac{\Delta}{2},$$

$$B_\phi(R) = -\frac{2\pi j_0}{cR}\{\frac{1}{2}(r - \frac{\Delta}{2})^2 - (\frac{\Delta}{\pi})^2 + \frac{R^2}{2}$$
$$+ \frac{\Delta R}{\pi}\sin[\frac{\pi}{\Delta}(R - r + \frac{\Delta}{2})]$$
$$+ (\frac{\Delta}{\pi})^2\cos[\frac{\pi}{\Delta}(R - r + \frac{\Delta}{2})]\},$$
$$r - \frac{\Delta}{2} < R \leq r + \frac{\Delta}{2},$$

$$B_\phi(R) = -\frac{2\pi j_0}{cR}[r^2 + (\frac{\Delta}{2})^2 - 2(\frac{\Delta}{\pi})^2], \quad R > r + \frac{\Delta}{2}, \tag{9}$$

r being the radius of the FR, Δ the thickness of the transition layer between the FR and the corona, and j_0 is the electric current density inside the FR.

Given the spatial distribution of the current density:

$$j(R) = j_0, \; 0 \leq R \leq r - \frac{\Delta}{2},$$

$$j(R) = \frac{j_0}{2}\{\cos[\frac{\pi}{\Delta}[R - r + \frac{\Delta}{2}] + 1\},$$

$$r - \frac{\Delta}{2} < R \leq r + \frac{\Delta}{2},$$

$$j(R) = 0, \; R > r + \frac{\Delta}{2}, \tag{10}$$

the initial pressure inside the FR in equilibrium with its neighbourhood results in

$$p = p_0 - \frac{1}{c} \int_R^\infty B_\phi(R') j(R') \, dR', \tag{11}$$

where p_0 is the background pressure. We obtain the FR density assuming different plasma temperatures T_{fr}, which can be either higher or lower than the coronal temperature T_c, depending on whether the FR is hot (Aparna & Tripathi 2016; Fan 2016) or cold (Ciaravella et al. 2000; Mei et al. 2012). In the following analysis, for comparison, we consider three FR temperatures: 0.1 MK, 1 MK and 10 MK, which we refer as the cold, tepid and hot cases, respectively. Note that the tepid case corresponds to the coronal ambient temperature.

We consider a stratified atmosphere due to gravity in order to satisfy the hydrostatic equilibrium of the background environment. The gravity in the vertical direction is

$$g = \frac{-G M_\odot}{(y + R_\odot)^2}, \tag{12}$$

with G the gravitational constant, $M_\odot = 1.989 \times 10^{33}$ g the mass of the Sun and $R_\odot = 696.3$ Mm the solar radius. On the other hand, to analyse the effects of coronal waves on the chromosphere we model three different atmosphere regions, a lower layer representing the chromosphere of height $h_{chr} = 2000$ km, followed by the transition region of width $w_{tr} = 500$ km and the corona. The thermodynamic properties are set considering an isothermal corona of temperature $T_c = 10^6$ K, an isothermal chromosphere of temperature $T_{chr} = 5000$ K, and a linear temperature variation in the transition region connecting the other two regions. The pressure and the density are obtained considering the hydrostatic equilibrium, $dp/dy = -\rho g$, where the density and pressure reference values are calculated at the coronal base assuming a fixed number density, n_c, and a given temperature, T_c.

In the proposed model, the atmosphere and the background magnetic field are in total equilibrium, except for the unstable FR-like prominence (or filament) that triggers the CME. The equilibrium of this system can be analysed considering a generalized potential energy. Near the equilibrium state the system varies quasi-statically in response to slow changes of the parameters M and j_0, but for certain critical points a catastrophic loss of equilibrium occurs (Forbes 1990). We here start with the state of the system, t_0, that is already out of equilibrium (Wang et al. 2009), the time when the Lorentz forces surpass the gravity force.

2.1 Numerical code

In order to evaluate the plasma behaviour, equations (1)–(4) are numerically solved. For the simulations we use the finite-volume

Table 1. Initial values of the parameters needed to set the initial condition. The radius of the FR is r, the height of the FR is h_0, the depth of the line dipole below the boundary surface is d, the thickness of the transition layer between the FR and the corona is Δ, the relative intensity of the dipole is M, the coronal temperature is T_c, the chromospheric temperature is T_{chr}, the numerical density at the base of the corona is n_c, the chromospheric height is h_{chr} and the transition region width is w_{tr}. The electric current density j_0 and the temperature T_{fr} of the FR are the control parameters.

Parameter	Value
r	2500 km
h_0	6250 km
d	3125 km
Δ	1250 km
M	1
T_c	10^6 K
T_{chr}	5000 K
n_c	1.2×10^8 cm^{-3}
h_{chr}	2000 km
w_{tr}	500 km

FLASH Code (Fryxell et al. 2000) that solves the compressible MHD equations with adaptive mesh refinement (AMR) and message passing interface (MPI) capabilities. We choose the 'unsplit staggered mesh' (USM) scheme (Lee, Deane & Federrath 2009) available in FLASH, which uses a high-resolution finite-volume method with a directionally unsplit data reconstruction and the constraint transport method (CT) to enforce the divergence-free condition of the magnetic field. The Riemann problems in the cell interfaces are calculated by the multistate Harten–Lax–van Leer Discontinuities (HLLD) Riemann solver (Miyoshi & Kusano 2005).

Cartesian 2D AMR grids are used to represent the physical domain of $[-250, 250]$ Mm $\times$ $[0, 250]$ Mm with a initial 20×10 discretization and eight refinement levels, taking into account the variation of the pressure, the density and the magnetic field. This results in a maximum resolution of 200×200 km, which allows us to model the chromosphere with a resolution of 10 cells and the transition region with 3 cells in the y-direction for the parameters of Table 1. Boundary conditions are set as follows. At both lateral ends outflow conditions (zero-gradient) are applied for thermodynamic variables and velocity, allowing waves to leave the domain without reflection, whereas the magnetic field requires extrapolation of the initial configuration to ghost cells in order to avoid the generation of spurious magnetic forces produced with outflow conditions. Obviously, this model is valid as long as shocks or disturbances do not reach the lateral ends of the domain. In the lower and upper limits the hydrostatic boundary conditions proposed by Fuchs et al. (2010) are implemented to guarantee the conservation of the hydrostatic equilibrium at both ends. In addition, to ensure the line-tied magnetic field condition in the solar surface during the CME evolution, at the bottom we implement the boundary condition described by Robertson & Priest (1987).

The capability of the code to preserve hydrostatic equilibrium in the whole domain must be taken into account. This is essential when strong gradients of hydrostatic pressure are present, as occurs between the chromosphere and the transition region. As the FLASH code uses a type-MUSCL scheme, even using high-order
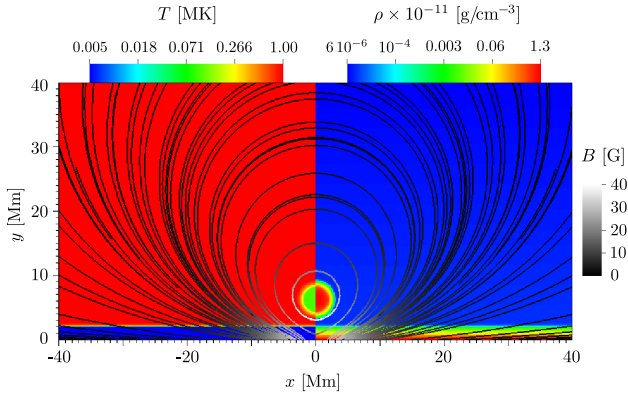
Figure 1. Initial configurations of the plasma temperature distribution (for $x < 0$), density distribution (for $x > 0$) and the magnetic field lines (the image is zoomed-in) with $j_0 = 1000\,\text{statA}\,\text{cm}^{-2}$ and $T_{\text{fr}} = 0.1\,\text{MK}$.

reconstructions of the interface pressure, spurious accelerations appear in the stratified atmosphere (Zingale et al. 2002; Käppeli & Mishra 2016). Although these effects can be reduced, improving the resolution of the grid, the present configuration does not allow this strategy because of the strong hydrostatic pressure gradients; i.e. the chromosphere is a very small part of the domain. Thus, a fine enough grid in the chromosphere will produce too dense a mesh with a consequent increment of the computational requirements, even when AMR capabilities are used. To obtain a well balanced code considering the initial force-free condition at the domain ends we here implemented the second-order hydrostatic reconstruction scheme proposed by Fuchs et al. (2010). Although this reconstruction is not strictly well balanced for atmospheres with variable temperature, the scheme behaves well enough, avoiding strong spurious accelerations.

2.2 Initial condition

In Table 1 we list the parameters used to set the initial condition of Eqs. (7)–(11). Parameters j_0 and T_{fr} are control variables used as the independent variables in the study of the triggering and propagation of Moreton waves.

In Fig. 1 we show the initial configuration of the magnetic field lines and the plasma density distribution in regions close to the FR. Here we start with a pseudo-equilibrium condition where the internal pressure of the FR equilibrates the magnetic pressure and the initial velocity is zero in the whole domain. Note that in this initial configuration, in contrast with the model proposed in Vršnak et al. (2016), it is not necessary to force the eruption of the FR, but it is triggered by the imbalance between the force due to the magnetic tension and the gravity force (weight) in the y-direction.

2.3 Diffusion effects

We include the anisotropic thermal conduction of Spitzer (1962), whose thermal flux is locally split into its parallel and perpendicular components with respect to the magnetic field,

$$\boldsymbol{Q} = -\kappa_\parallel (\nabla T)_\parallel - \kappa_\perp (\nabla T)_\perp, \tag{13}$$

where $\kappa_\parallel$ and $\kappa_\perp$ are thermal conductivities along and across the magnetic field direction, while $(\nabla T)_\parallel$ and $(\nabla T)_\perp$ are the corresponding temperature gradients. Because $\kappa_\parallel \gg \kappa_\perp$ with $\kappa_\perp$ being very small, the heat flux is mostly funnelled along the field direction and highly inhibited perpendicular to it (see e.g. Zurbriggen et al.
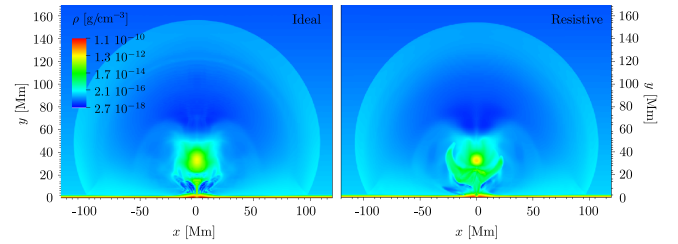

Figure 2. Plasma density distribution at $t = 200\,\text{s}$ with $j_0 = 2000\,\text{statA}\,\text{cm}^{-2}$ and $T_{\text{fr}} = 1\,\text{MK}$. The left-hand panel corresponds to an ideal MHD simulation and the right-hand panel to a resistive MHD one.
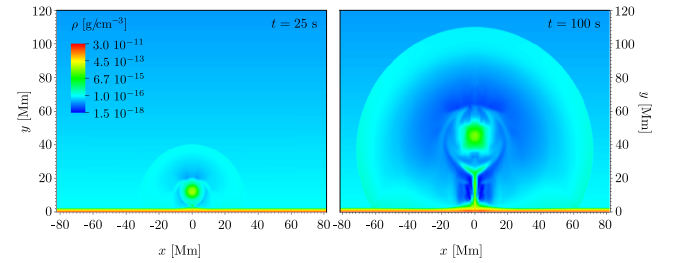

Figure 3. Evolution of the plasma density for $j_0 = 1000\,\text{statA}\,\text{cm}^{-2}$ and the parameters of Table 1 with an FR temperature of 10 MK. The domain has been reduced to highlight the evolution near the FR.

(2016) and references therein). Performing a few runs for short time intervals (up to $\sim$1 min), we conclude that the heat conduction is inefficient to modify the FR evolution due to its closed magnetic configuration (Fig. 1), where the heat interchange between the FR and its surroundings is null.

We also consider magnetic resistivity to simulate reconnections at current sheet locations while the FR rises. For this purpose, we set a uniform physical magnetic diffusivity of $\eta = 5 \times 10^9\,\text{cm}^2\,\text{s}^{-1}$ in the small region below the FR, where the magnetic field lines of opposite polarities increase due to the stretching of the field lines. Outside the region of the current sheet we assume that the magnetic diffusivity is zero ($\eta = 0$). Fig. 2 shows the FR evolution at time $t = 200\,\text{s}$ with $j_0 = 2000\,\text{statA}\,\text{cm}^{-2}$ and $T_{\text{fr}} = 1\,\text{MK}$, without resistivity (left-hand panel) and with resistivity (right-hand panel). For different trials, we obtain that the rise speed and the position of the FR, as a function of time, are almost the same for these two cases. Thus, we neglect the resistivity and heat conduction terms, keeping the ideal MHD equations, i.e. $\boldsymbol{Q} = 0$ and $\eta = 0$.

3 RESULTS AND DISCUSSION

3.1 CME mechanism

In Fig. 3 we schematize the dynamics of the FR that starts to rise provided that the magnetic field forces surpass the FR weight. We plot the density at different times for the parameters of Table 1, a current density of $j_0 = 1000\,\text{statA}\,\text{cm}^{-2}$ and an internal FR temperature of 10 MK (hot case). In the figure we show that a fast magnetosonic shock is generated around the FR by both the projectile and piston effects. The FR lift-off also produces a chromospheric depression (not detectable in the figure) that induces a travelling perturbation that advances in the horizontal direction. As will be seen, depending on the initial setup values this perturbation will give rise to the Moreton wave formation.
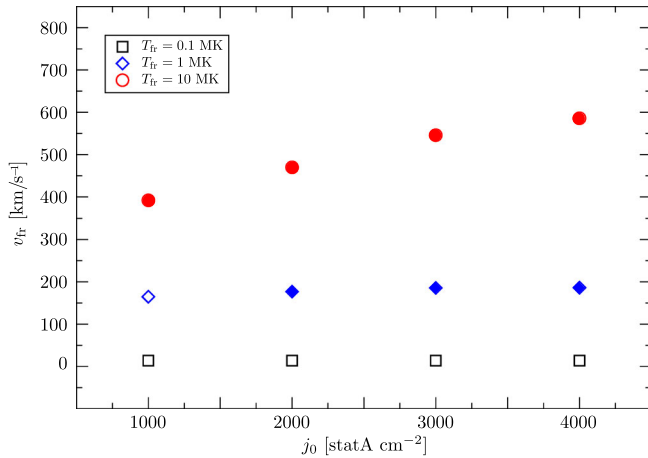
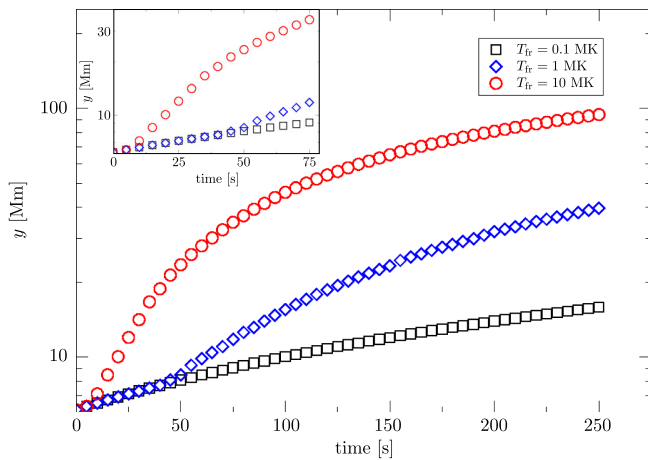**Figure 4.** FR velocities v_{fr} as a function of j_0 for all the FR temperatures here considered.

Figure 5. FR position in the *y*-direction as a function of time for $j_0 = 1000 \, \text{statA} \, \text{cm}^{-2}$ and all the FR temperatures considered.

The FR temperature defines the acceleration of the FR in the *y*-direction. That is, due to equation (11) the initial internal pressure is assumed to be in equilibrium with the neighbourhood magnetic pressure. Thus, for a given pressure the equation of state determines that higher temperatures are associated with lower densities, i.e. lighter FRs. As mentioned, we choose three different values for the internal temperature that emulate a cold, tepid and hot FR (Ciaravella et al. 2000; Nindos et al. 2015; Aparna & Tripathi 2016). Fig. 4 shows that while the temperature increases for a given j_0 value, the speed of the FR also increases. The velocity values were obtained following the evolution of the FR centre (at the pressure peak) at $t = 180 \, \text{s}$, after the system speeds have reached a stable regime (see Fig. 5). Note that for the hot case an increase of j_0 implies a significant increase of the speed (for j_0 ranging between 1000–4000 statA cm^{-2} the speed increases $\sim 200 \, \text{km} \, \text{s}^{-1}$), but for the cold case, the speed remains almost constant for the same j_0 increment.

The acceleration and the rise speed of the FR also depend on the magnetic field strength, which is modified through the control parameter j_0. In Table 2, we show for different j_0 and FR temperatures, at time $t = 100 \, \text{s}$, different magnetic field strength values. One of them is the maximum value of the magnetic field strength achieved at a position below the FR located at the upper chromospheric sur-

Table 2. Maximum magnetic field strength and magnetic field strength at $(x, y) = (30, 5) \, \text{Mm}$ at $t = 100 \, \text{s}$.

j_0 [statA cm^{-2}]	T_{fr} [MK]	B [G]	B_{max} [G]
1000	0.1	2.3	57.8
1000	10	3.2	30.2
4000	0.1	9.7	232.6
4000	10	12.7	147.4
5500	5	19.3	292.7
8000	2.5	27.6	425.7
9000	1	33.0	479.0

face, where it is assumed that the magnetogram measurements are obtained (Balasubramaniam et al. 2010). To give a reference value of the coronal magnetic field strength in the neighbourhood of the FR we show other values at $(x, y) = (30, 5) \, \text{Mm}$.

To study the evolution of the FR speed, in Fig. 5 we plot the FR position in the *y*-direction as a function of time for the three temperature cases for $j_0 = 1000 \, \text{statA} \, \text{cm}^{-2}$ (the evolutions for the other values of j_0 are similar). The figure shows that the tepid and hot cases have similar behaviours, beginning with a strong acceleration (distinguished in the inset, e.g. lasting $\sim 5 \, \text{s}$ for the hot case); a subsequent deceleration stage of $\sim 145 \, \text{s}$ (for the hot case) leads to a final approximately constant speed stage starting at $t \gtrsim 150 \, \text{s}$. The cold FR case has an almost constant rise speed with a vanishing acceleration.

Depending on the final upward constant FR speed a coronal shock can be developed due to the combined projectile and piston mechanisms. The FR rising can initiate a bow-shock configuration (projectile mechanism) and while it rises the imbalance of the inner FR pressure with respect to that of the stratified environment can trigger the FR expansion (piston mechanism). Fig. 6 shows the plasma density features for $j_0 = 1000 \, \text{statA} \, \text{cm}^{-2}$, at time $t = 50 \, \text{s}$ and two different FR temperature values: the cold (left-hand panel) and hot (middle panel) cases, respectively. Note the presence of a fast magnetosonic shock wave for the hot case, which is absent for the cold one. This can be clearly seen in the right-hand panel showing the density along cuts of the two configurations: in red the density profile along the cut superimposed on the left-hand panel, and in blue the density profile along the cut superimposed on the middle panel. The density enhancement is clearly seen in the blue line and is difficult to identify in the red one (see the arrows in the figure). The evolution shows that while the heavier FR delays its lift-off, and consequently its expansion, the lightweight one has travelled a long distance in the corona, experiencing a strong expansion. Note from the figure that the expansion shock – featured by an approximately *spherical* geometry – dominates the dynamics of the hot case. In contrast, the cold FR remains almost quiescent with a balanced pressure (since the total pressure is initially in equilibrium); later a weak expansion is produced. The expansion of the hot FR that occurs when the internal pressure surpasses the external one (due to the exponential ambient pressure decay) can eventually lead to a spherical shock wave travelling radially from its centre, i.e. the so-called overexpansion.

When the expansion front reaches the transition region its denser plasma produces a strong deceleration of the expansion speed in the *y*-direction, but in the *x*-direction this speed is not reduced, inducing the wave sweeping of the chromospheric surface (see Fig. 3). Although a bow-shock (if present) is not directly related to the perturbation of the chromosphere, it is certainly an indicator of a large FR rise speed. Larger FR speeds result in stronger FR expansions because the imbalance between the internal pressure and the
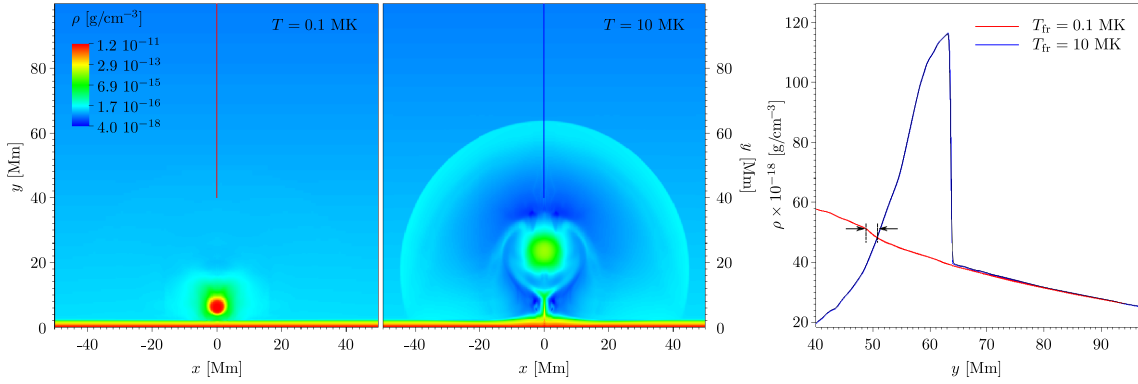
Figure 6. Density pattern of two FR configurations at time $t = 50$ s: (left-hand panel) 0.1 MK and (middle panel) 10 MK. The right-hand panel displays the density profile along the vertical cuts shown in the left-hand panel (red) and in the middle panel (blue).
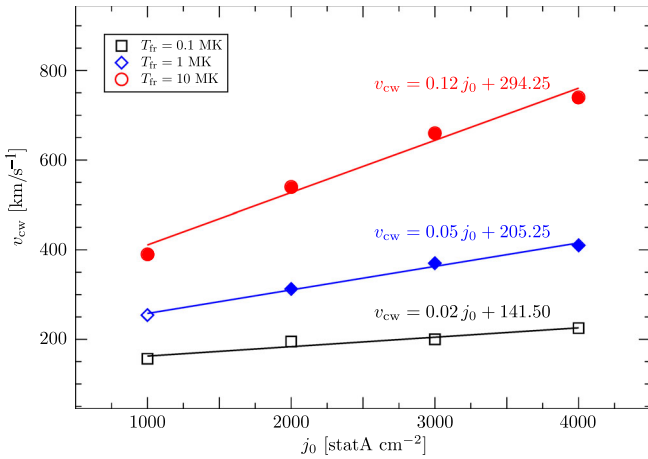

Figure 7. Coronal wavefront velocities in the x-direction v_{cw} as a function of j_0 for all the FR temperatures considered.

declining ambient one will be larger. To distinguish the cases with shocks from those without them, in Fig. 4 we indicate with filled marks the cases with a shock and with unfilled marks the cases without a definite one. From the figure we see that all the cases display a shock pattern, except for the $j_0 = 1000$ statA cm^{-2} tepid case and the almost static one with $v_{fr} \sim 10$ km s^{-1} for $T_{fr} = 0.1$ MK. A way to increase the rise speed is through the increase of the FR temperature in order to obtain a lighter FR.

As we are interested in the coronal wavefront that disturbs the chromosphere, in Fig. 7 we plot the wavefront speed of the FR expansion in the x-direction as a function of the current density j_0. The speed is measured at the base of the corona ($h = 2550$ km) at $t = 180$ s, when, for all cases, the wave has reached an almost constant speed. From Paper I we know that a sufficiently strong disturbance, i.e. a coronal shock wave, is required to produce a strong enough chromospheric density enhancement detectable by instruments. Also, considering that typical Moreton wave speeds (between ~400 km s^{-1} and 2000 km s^{-1}) are known to be of the fast magnetosonic type we analysed the Alfvénic Mach number M_A. Filled symbols in Fig. 7 indicate that a fast magnetosonic shock wave ($M_A > 1$) is produced whereas empty symbols account for sub-Alfvénic disturbances.

The figure shows, as expected, that cold FRs will not produce fast magnetosonic expanding shocks since they are too heavy. Only slow magnetosonic shocks are detected propagating upward in the y-direction. On the other hand, hot FRs are capable of generating

fast magnetosonic expanding shock waves with speeds increasing with j_0. For the tepid case, $M_A \lesssim 1$ for $j_0 < 2000$ statA cm^{-2} and $M_A \gtrsim 1$ for $j_0 \geq 2000$ statA cm^{-2}. Note that, in agreement with the Moreton wave observational values, the speeds corresponding to fast magnetosonic shock waves are in the range $\gtrsim 350$ km s^{-1}. This suggests that a combination of relatively large internal FR temperatures and relatively large magnetic field strengths are required to obtain a detectable Moreton wave. The argument that the overexpansion of the FR is the main mechanism producing shock waves in the base of the corona is reinforced by the analysis of Fig. 7. As the internal pressure of the FR increases with the magnetic field strength, the expansion will be larger for larger values of j_0, leading to larger shock speed, as seen from the figure. In contrast, Fig. 4 shows that the rise speed of the FR – and the bow-shock speed (if present) – remains constant or increases less than the increase of the shock speed at the coronal base, suggesting that the bow-shock does not significantly contribute to the Moreton wave formation. We conclude that only CME configurations with hot and tepid FRs and relatively strong magnetic fields are candidates for the production of Moreton waves.

3.2 Moreton formation and propagation

Fig. 8 displays the density profiles for different times ($t = 150, 200, 250$ s) as a function of the x-coordinate for two different heights: (upper panel) at a coronal altitude of 2550 km and (bottom panel) at an upper chromospheric height of 1500 km, where the Hα emission is produced (Vernazza, Avrett & Loeser 1981; Leenaarts, Carlsson & Rouppe van der Voort 2012). From the figure we note a delay between the coronal fast magnetosonic shock that sweeps the chromospheric surface and the compressional wave registered at the chromosphere, which is consistent with the geometry of the expansion whose curvature radius increases continuously (see Paper I for details). The wave that travels through the chromosphere is followed by a density decrease associated with the expansion caused by the rising of the FR.

When processing the Hα images in Francile et al. (2013) we determined that an ~8 per cent threshold in the intensity contrast of the running difference images was required to detect a Moreton perturbation, i.e. lower threshold values were not reliable due to the high noise levels of the data. Leenaarts et al. (2012) show that the optical depth in the upper chromosphere is proportional to the column mass so the brightness is linearly related to the plasma density. In this case, besides the density increase, there will be an additional contribution to the Hα intensity due to the Doppler shift
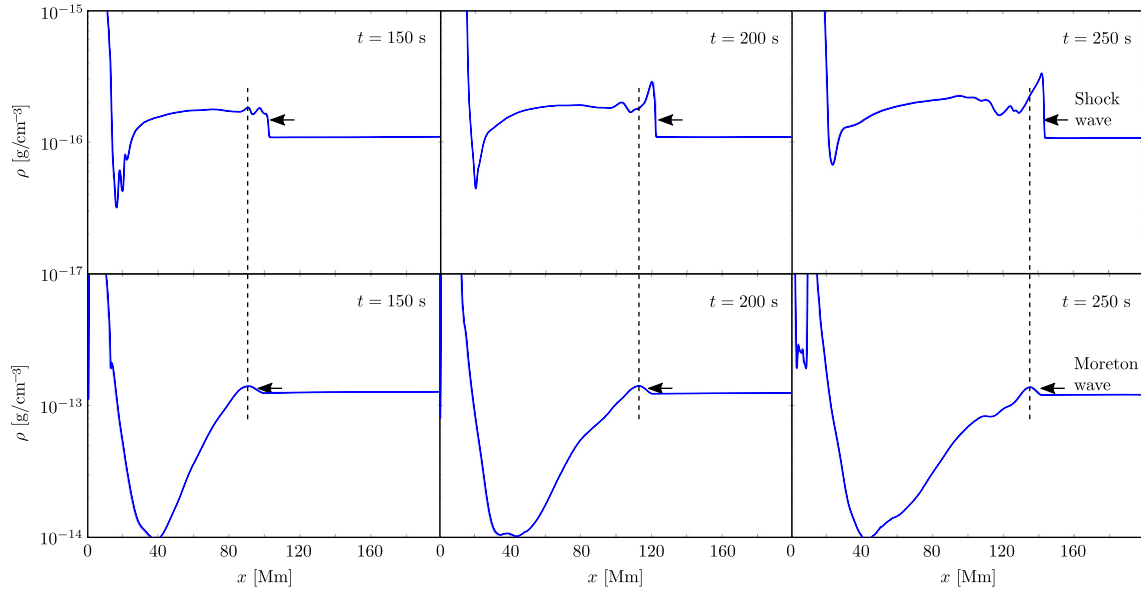
Figure 8. Density profiles in the corona–chromosphere interface ($h = 2550$ km) (upper panels) and in the upper chromosphere ($h = 1500$ km) (lower panels) for $j_0 = 4000$ statA cm^{-2}, $T_{\rm fr} = 1$ MK and the parameters of Table 1.
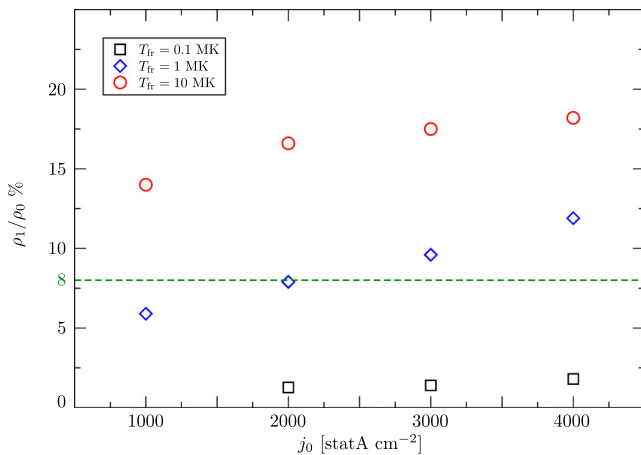

Figure 9. Chromospheric compression density ratio ρ_1/ρ_0 as a function of j_0 for all the FR temperature values considered.

(Moreton 1964) and Doppler brightening effect (Rompolt 1980) of the line due to the radial speed originating in the compression of the chromosphere. The Moreton propagation shifts the Hα line with respect to the filter passband, resulting in an intensity increase in the line core as well as in the blue line wing, and an intensity decrease in the red wing. Thus we here impose an upper limit to the density of ~8 per cent as the minimum density contrast required to detect a chromospheric Moreton wave. This threshold explains the distance without wave perturbations between the radiant point (the probable location of the single wave source projected into the chromosphere) and the place where the Moreton wave is initially visible.

Fig. 9 displays the chromospheric compression density ratio (ρ_1/ρ_0, ρ_0 the background density and ρ_1 the maximum density perturbation at height $y = 1500$ km and $t = 180$ s) for the different temperature cases as a function of j_0. The dotted line indicates the ~8 per cent compression density limit above which we consider that the chromospheric perturbation is detected as a Moreton wave. Note that only the cases that lead to a fast magnetosonic shock for-

mation close to the upper chromospheric surface will account for an observable Moreton perturbation (see Fig. 7).

The rarity of the Moreton wave observations with respect to the numerous CME events could be explained by the small number (~1 per cent) of coronal shocks driven by CMEs (Gopalswamy 2006). Thus, in the frame of our scenario, the CME with a sufficiently rapid lift-off that leads to a strong expansion of the FR would be a necessary requirement to produce a detectable Moreton wave. Indirectly, this would imply the presence of a fast bow-shock produced by the upward motion of the FR, since it would indicate a rapid rise and consequently a strong expansion.

In order to study how the temperature of the FR and magnetic field strength affect the kinematics of a chromospheric perturbation, in Fig. 10 we show the chromospheric distance travelled by the Moreton wave for different values of the FR temperature ($T_{\rm fr} = 1, 2.5, 5, 10$ MK) and the electric current density ($j_0 = 2000, 4000, 5500, 8000, 9000$ statA cm^{-2}). The symbols in this figure represent the position of a density enhancement equal or greater than 8 per cent that moves away from the initial position of the FR in the x-direction. As stated above, the density perturbation is measured in the upper chromosphere, at $h = 1500$ Mm. The delay between the coronal triggering time and the onset of the Moreton wave is due to the time that it takes the shock front to reach the upper chromosphere plus the time that it takes the density compression ratio to surpass the ~8 per cent threshold. As observed in the figures, the delay of the Moreton onset is in the range of 30 s to 150 s corresponding to distances ranging from 30 Mm to 100 Mm, respectively. These distances are consistent with observed minimum distances for Moreton waves as reported by Warmuth et al. (2004a) and Narukage et al. (2008). The figure shows that the larger the current density, the shorter the delay time (upper panel), and that the larger the FR temperature, the shorter the travelled distance to surpass the required density threshold (bottom panel). The speed of the Moreton wave is given by the slopes in Fig. 10 and is determined by both parameters. Note that, as expected, the hotter the FR (lighter) and the larger the current density the faster the Moreton wave. In accordance with most observations, our simulations
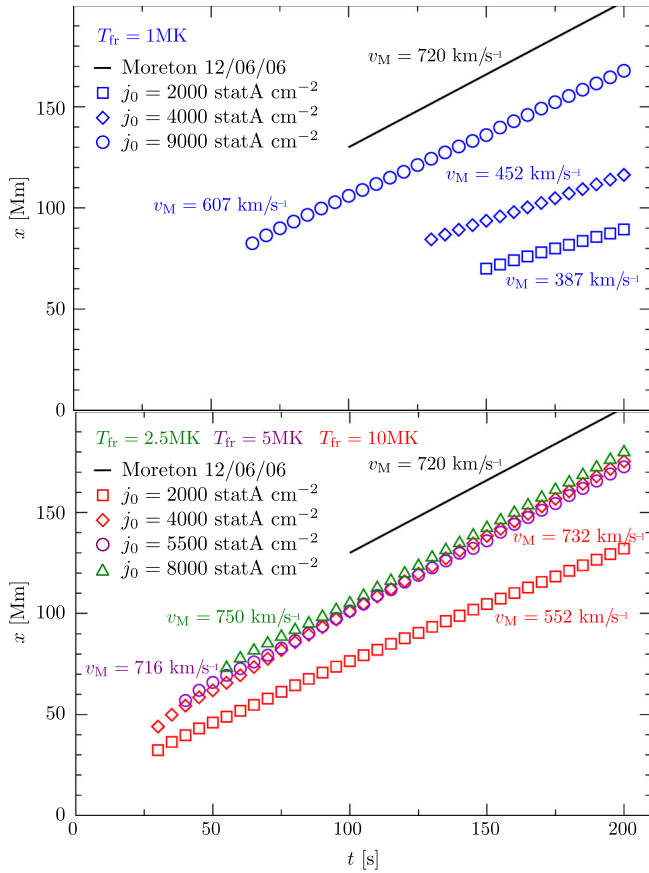
Figure 10. Chromospheric distance travelled by a Moreton wave as a function of time. The upper panel displays the results obtained with $T_{fr} = 1$ MK and $j_0 = 2000$ statA cm^{-2} in blue squares, $j_0 = 4000$ statA cm^{-2} in blue diamonds and $j_0 = 9000$ statA cm^{-2} in blue circles. The bottom panel displays the results obtained with $T_{fr} = 2.5$ MK and $j_0 = 8000$ statA cm^{-2} in green triangles, $T_{fr} = 5$ MK and $j_0 = 5000$ statA cm^{-2} in violet circles, $T_{fr} = 10$ MK and $j_0 = 2000$ statA cm^{-2} in red squares and $j_0 = 4000$ statA cm^{-2} in red diamonds. In both panels, the solid black line represents the chromospheric distance travelled by the Moreton wave of the 2006 December 6 event.

show that the speeds of detectable Moreton waves are greater than $\sim$400 km s^{-1}.

The solid line of Fig. 10 represents the evolution of the Moreton wave of 2006 December 6. The wave registered an average speed of 732 km s^{-1} with a delay time of about 130 s at a distance of $\sim$100 Mm (Francile et al. 2013). Our numerical results are able to capture many of the kinematic features of the phenomenon, i.e. the Moreton wave speed (when hot FRs are considered) and the density chromospheric profiles (see Fig. 8). The delay of the space–time location in the numerical results with respect to the observational data could be adjusted modifying the parameters of Table 1, such as the initial altitude h_0 of the FR and the dipole parameter d, for each of the particular combinations of FR temperatures and j_0 values.

4 CONCLUSIONS

In Paper I, we numerically showed, using as a case study the 2006 December 6 event, that the action of a piston mechanism emulating either a flare-ignited blast wave (simulated as an instantaneous pressure pulse) or the flank expansion of a CME (simulated as a temporary pressure pulse) could be responsible for the formation of Moreton waves. We established that to obtain a sufficiently strong

coronal shock (able to generate detectable chromospheric waves) a relatively low magnetic field strength is required in comparison with that registered in active regions. However, a low magnetic field strength leads to a slow Alfvén speed and thus to a slower coronal shock. Thus, although the blast wave scenario could reproduce the 2006 December 6 event, it could not explain higher-speed events such as the 2014 March 29 Moreton wave (Francile et al. 2016).

In this work we numerically evaluated the capability of a CME event to produce Moreton waves considering a pseudo-equilibrium model that treats the current-carrying filament floating in the corona as a flux rope (FR) located at a certain height from the solar surface. Although in a real CME the reconnection process could actually influence the kinematics of the eruption (see e.g. Lin et al. 2005), we here assumed that the rearrangement of the magnetic field through reconnection processes in the current sheet does not determine the CME dynamics.

For this model the eruption arises from the imbalance between the magnetic tension in the y-direction and the gravity force. This constitutes a key difference with respect to other models that propose initial configurations with internal overpressure values in the FR (e.g. Vršnak et al. 2016).

In contrast with the blast wave scenario analysed in Paper I, we show that the coronal shock, which results from the FR overexpansion, increases its strength when the magnetic field is increased (controlled through the parameter j_0) if high enough temperatures inside the FR are considered. This is because the overexpansion is due to the loss of the equilibrium balance between the FR internal pressure and the total external one. Thus, taking into account that the stronger the magnetic field, the faster the FR rise in the direction of declining pressures, this results in the strength of the expanding waves increasing with the strength of the magnetic field. In addition, the large rise speed of the FR makes strong expanding coronal shocks appear together with bow-shock-type features moving ahead of the FR.

In agreement with Vršnak et al. (2004), Temmer et al. (2009) and Vršnak et al. (2016), considering a scenario where the initial configuration is in pseudo-equilibrium, we show that only strong lateral expansions of FRs leading to fast magnetosonic coronal shocks are able to sweep the chromospheric surface producing detectable Moreton waves. Varying the control parameters that define the FR temperature and the magnetic field strength we find that the resulting Moreton waves (when present) exhibit the main kinematic features of the observed events. Therefore, we conclude that only very impulsive CMEs, i.e. configurations with hot FRs and relatively strong magnetic fields that lead to an FR overexpansion, could generate detectable chromospheric disturbances. However, it should be taken into account that although the piston mechanism that produces the required expansion would be responsible by itself for the Moreton wave generation, bow-shock features could be present, as they are a consequence of large FR rise speeds (Francile et al. 2016).

REFERENCES

Aparna V., Tripathi D., 2016, ApJ, 819, 71
Asai A. et al., 2012, ApJ, 745, L18
Balasubramaniam K. S. et al., 2010, ApJ, 723, 587
Chen P. F., Wu Y., 2011, ApJ, 732, L20
Chen P. F., Ding M. D., Fang C., 2005, Space Sci. Rev., 121, 201
Ciaravella A. et al., 2000, ApJ, 529, 575
Fan Y., 2016, ApJ, 824, 93
Forbes T., 1990, J. Geophys. Res., 95, 11919
Francile C., Costa A., Luoni M. L., Elaskar S., 2013, A&A, 552, A3
Francile C., López F. M., Cremades H., Mandrini C. H., Luoni M. L., Long D. M., 2016, Sol. Phys., 291, 3217
Fryxell B. et al., 2000, ApJS, 131, 273
Fuchs F. G., McMurry A. D., Mishra S., Risebro N. H., Waagan K., 2010, J. Comput. Phys., 229, 4033
Gopalswamy N., 2006, Washington DC American Geophysical Union Geophysical Monograph Series, 165, 207
Käppeli R., Mishra S., 2016, A&A, 587, A94
Klassen A., Aurass H., Mann G., Thompson B. J., 2000, A&AS, 141, 357
Kleint L., Battaglia M., Reardon K., Sainz Dalda A., Young P. R., Krucker S., 2015, ApJ, 806, 9
Krause G., Cécere M., Francile C., Costa A., Elaskar S., Schneiter M., 2015, MNRAS, 453, 2799
Lee D., Deane A. E., Federrath C., 2009, in Pogorelov N. V., Audit E., Colella P., Zank G. P., eds, ASP Conf. Ser. Vol. 406, Numerical Modeling of Space Plasma Flows: ASTRONUM-2008. Astron. Soc. Pac., San Francisco, p. 243
Leenaarts J., Carlsson M., Rouppe van der Voort L., 2012, ApJ, 749, 136
Lin J., Ko Y.-K., Sui L., Raymond J. C., Stenborg G. A., Jiang Y., Zhao S., Mancuso S., 2005, ApJ, 622, 1251
Liu C. et al., 2015, ApJ, 812, L19
Liu W., Nitta N. V., Schrijver C. J., Title A. M., Tarbell T. D., 2010, ApJ, 723, L53
Magdalenić J., Marqué C., Zhukov A. N., Vršnak B., Veronig A., 2012, ApJ, 746, 152
Mei Z., Shen C., Wu N., Lin J., Murphy N. A., Roussev I. I., 2012, MNRAS, 425, 2824
Miyoshi T., Kusano K., 2005, J. Comput. Phys., 208, 315

Moreton G. E., 1960, AJ, 65, 494
Moreton G. F., 1964, AJ, 69, 145
Narukage N., Ishii T. T., Nagata S., UeNo S., Kitai R., Kurokawa H., Akioka M., Shibata K., 2008, ApJ, 684, L45
Nindos A., Patsourakos S., Vourlidas A., Tagikas C., 2015, ApJ, 808, 117
Robertson J. A., Priest E. R., 1987, Sol. Phys., 114, 311
Rompolt B., 1980, Hvar Obser. Bull., 4, 39
Shen Y., Liu Y., 2012, ApJ, 752, L23
Spitzer L., 1962, Physics of Fully Ionized Gases, 2nd edn. Interscience, New York
Su W., Cheng X., Ding M. D., Chen P. F., Sun J. Q., 2015, ApJ, 804, 88
Temmer M., Vršnak B., Žic T., Veronig A. M., 2009, ApJ, 702, 1343
Uchida Y., 1968, Sol. Phys., 4, 30
Uchida Y., Altschuler M. D., Newkirk G., Jr, 1973, Sol. Phys., 28, 495
Vernazza J. E., Avrett E. H., Loeser R., 1981, ApJS, 45, 635
Vršnak B., Cliver E. W., 2008, Sol. Phys., 253, 215
Vršnak B., Warmuth A., Brajša R., Hanslmeier A., 2002, A&A, 394, 299
Vršnak B., Maričić D., Stanger A. L., Veronig A., 2004, Sol. Phys., 225, 355
Vršnak B., Warmuth A., Temmer M., Veronig A., Magdalenić J., Hillaris A., Karlický M., 2006, A&A, 448, 739
Vršnak B., Žic T., Lulić S., Temmer M., Veronig A. M., 2016, Sol. Phys., 291, 89
Wang H., Shen C., Lin J., 2009, ApJ, 700, 1716
Wang H., Liu S., Gong J., Wu N., Lin J., 2015, ApJ, 805, 114
Warmuth A., 2010, Advances Space Res., 45, 527
Warmuth A., Vršnak B., Aurass H., Hanslmeier A., 2001, ApJ, 560, L105
Warmuth A., Vršnak B., Magdalenić J., Hanslmeier A., Otruba W., 2004a, A&A, 418, 1101
Warmuth A., Vršnak B., Magdalenić J., Hanslmeier A., Otruba W., 2004b, A&A, 418, 1117
Warmuth A., Mann G., Aurass H., 2005, ApJ, 626, L121
Wu S. T., Wu C.-C., Liou K., 2013, in Pogorelov N. V., Audit E., Zank G. P., eds, ASP Conf. Ser. Vol. 474, Numerical Modeling of Space Plasma Flows (ASTRONUM2012). Astron. Soc. Pac., San Francisco, p. 185
Zingale M. et al., 2002, ApJS, 143, 539
Zucca P., Pick M., Démoulin P., Kerdraon A., Lecacheux A., Gallagher P. T., 2014, ApJ, 795, 68
Zurbriggen E., Costa A., Esquivel A., Schneiter M., Cécere M., 2016, ApJ, 832, 74

This paper has been typeset from a TEX/LATEX file prepared by the author.